LASER & PHOTONICS REVIEWS

www.lpr-journal.org

Electrically Driven Tunable Broadband Polarization States via Active Metasurfaces Based on Joule-Heat-Induced Phase Transition of Vanadium Dioxide

Fang-Zhou Shu, Jia-Nan Wang, Ru-Wen Peng, Bo Xiong, Ren-Hao Fan, Ya-Jun Gao, Yongmin Liu,* Dong-Xiang Qi, and Mu Wang**

Broadband tuning of polarization states is pivotal yet challenging in modern photonics technologies, especially for miniaturized or integrated systems. Metasurfaces potentially provide an effective approach to resolve this challenge. However, once a metadevice is fabricated, its functionalities are determined, and it is hard to actively tune the polarization states. Here, the electrically tunable broadband polarization states by combining phase-change material (vanadium dioxide) and dispersion-free metasurface are demonstrated for the first time. The polarization states are modulated through the electrically driven, Joule-heat-induced phase transition of vanadium dioxide, where the output polarization state can be continuously tuned from horizontal one to vertical one, or from circular polarization to linear polarization. With accurate on-chip control of the phase transition, continuous and reversible modulation of polarization is verified in a scanning display. Moreover, a proof-of-concept demonstration for dynamically independent control of multiple polarization display is carried out. Different images are produced by applying electrical currents in *N* separate channels to generate a dynamic multiplexing polarization display with 2^N encoding states. Such an active metasurface can be readily integrated with electronics and has potential applications in display, encryption, camouflage, and information processing.

1. Introduction

Tuning the polarization states of light plays a crucial role in the classical optical system and modern photonics technology. However, the bulky volume of conventional waveplates made of birefringent materials is highly unfavorable for miniaturized optical systems and integrated photonic circuits. As an alternative, metasurfaces have attracted enormous attention over the past years because they have facilitated ultrathin optical devices[1–7] to tune the local amplitude, phase, and polarization of light on a 2D platform. Subwavelength waveplates based on metasurfaces have already been extensively investigated due to their compactness and design flexibility.[8-12] However, one major challenge limiting the application of these subwavelength waveplates is that their functionality is fixed after fabrication, imposing the challenge to exert any further active control on the polarization states of light.

To solve this problem, active metasurfaces have been recently developed to provide optical devices with both dynamic tunability and miniaturization.[13–15] The general method to produce active metasurfaces is to combine metasurfaces with some dynamically tunable elements, such as graphene,[16–18] semiconductors,[19] nonlinear materials,[20,21] phase-change materials,[22,23] liquid crystals,[24–26] field-programmable gate array (FPGA),[27] and some mechanical rotating structures.[28] Various active functionalities, including tunable polarization,[16,19–22,29] dynamic color display,[23,30] switchable reflection and transmission,[24,31] dynamic beam switching,[25] spatial light modulators,[26] and reconfigurable holograms[32,33] have been demonstrated. In these active optical devices, the optical properties can be dynamically controlled by certain external stimuli, including voltage, light, and heat, resulting in distinct responses under different conditions. Particularly, the refractive index of liquid crystals can be tuned optically,[24] thermally,[25] or electrically.[26] Therefore, liquid crystals are widely used to implement tunable metasurfaces.[24–26] Although some studies discuss tunable polarizers, their ability to be tuned is limited.[16,19–22] In particular, electrically tunable, broadband, and efficient wave plates have not yet been explored.

Dr. F.-Z. Shu, J.-N. Wang, Prof. R.-W. Peng, B. Xiong, Dr. R.-H. Fan, Y.-J. Gao, Dr. D.-X. Qi, Prof. M. Wang
National Laboratory of Solid State Microstructures
School of Physics, Collaborative Innovation Center of Advanced Microstructures
Nanjing University
Nanjing 210093, China
E-mail: rwpeng@nju.edu.cn; muwang@nju.edu.cn

Prof. Y. Liu
Department of Electrical and Computer Engineering
Northeastern University
Boston, MA 02115, USA
E-mail: y.liu@northeastern.edu

Prof. Y. Liu
Department of Mechanical and Industrial Engineering
Northeastern University
Boston, MA 02115, USA

Prof. M. Wang
American Physical Society
Ridge, NY 11961, USA

The ORCID identification number(s) for the author(s) of this article can be found under https://doi.org/10.1002/lpor.202100155

DOI: 10.1002/lpor.202100155

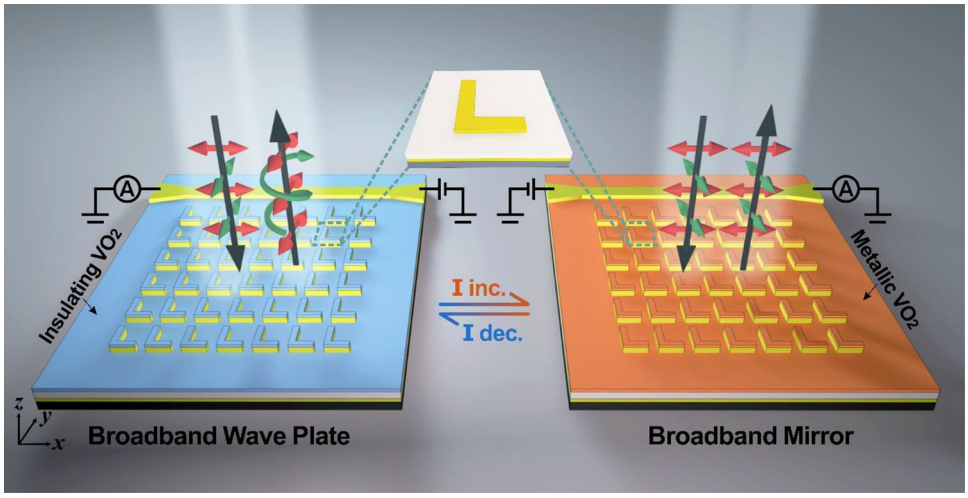

Figure 1. Schematic of electrically driven tunable broadband polarization states. The active metastructure is constructed by Si substrate, Au mirror layer, SiO_2 spacing layer, gold L patterns, and VO_2 layer (from bottom to top). The inset shows the model of a unit cell without being covered by VO_2. An electrode is fabricated near the metasurface, which is connected to external circuitry. When the applied current is lower than a critical value, the VO_2 is in the insulating phase, and the reflected light is transformed into a *y*-polarized light with *x*-polarized incidence (red arrows) or left-hand circularly polarized light with *y*-polarized incidence (green arrows) depending on the structural parameters. Therefore, the sample functions as a broadband half- or quarter-wave plate, as schematically shown in the left panel. When the current is increased, the VO_2 is transformed to the metallic phase, and the polarization state of reflected light remains the same as the *x*-/*y*-polarized incident light, indicating that the sample functions as a broadband mirror, as schematically shown in the right panel.

Phase-change materials are a category of active materials that can introduce tunability to metasurfaces. Among the diverse phase-transition materials, vanadium dioxide (VO_2) is particularly fascinating.[34,35] First, it is a reversible phase-change material with a low critical temperature of ≈340 K.[36] At room temperature (300 K), VO_2 is an insulator with a monoclinic structure. When the temperature increases above 340 K, it transforms into metal with a rutile structure. The phase transition causes a large change in the electrical and optical properties of VO_2. Consequently, it has been widely used in field-effect transistors,[37,38] actuators,[39,40] intelligent windows,[41] active metamaterials,[42–45] reconfigurable phase and polarization control,[22,29] dynamic color generation,[30] and waveguide switches.[46] Second, in addition to direct heating, the phase transition of VO_2 can also be induced by electric current,[47,48] strain,[49] and light,[50] which can greatly increase the range of modulation methods. Furthermore, in practical applications, electric modulation is more useful than temperature modulation due to its compatibility with electronics. However, there have been few studies on dynamically reversible metasurfaces that are based on electrically tuned phase transition of VO_2,[51–53] and only very limited work focuses on the active manipulation of amplitude[51,52] and phase.[53] The electrical control of polarization states is still lacking.

In this study, electrical tuning of broadband polarization states by combining VO_2 with dispersion-free metasurfaces is experimentally demonstrated for the first time. Based on the Joule-heat-induced phase transition of VO_2, the tunable broadband feature is achieved in subwavelength half-wave and quarter-wave plates, where the polarization state of the reflected light can be electrically tuned from a horizontal polarization to a perpendicular polarization, or from circular polarization to linear polarization. Moreover, by taking advantage of the precise and continuous electrical control, we realize a dynamically reversible infrared scanning display metadevice. As a proof-of-concept demonstration for dynamically independent control on the chip, multiple different images are produced by applying currents in N independent spatial channels, and a dynamic display with 2^N encoding states ($N = 3$ in our current experiments) is demonstrated, realizing a dynamic multiplexing polarization display. Our work combines dispersion-free metasurfaces and phase-change materials, providing a new platform to produce electrically tunable broadband metadevices and inspiring further applications in optical display, encryption, and information communication.

2. Results

2.1. Electrically Tuning Broadband Polarization States

To tune dynamically broadband polarization states, we designed an anisotropic dispersion-free metasurface that was integrated with the phase change material (VO_2) as shown in the schematic in **Figure 1**. The metasurface uses a metal-insulator-metal (MIM) structure[3,9–12] to achieve broadband functionality, in which an array of anisotropic Au "L" nanoantenna is introduced to support distinct modes as described previously.[11,12] In this configuration, the dispersion of the resonant modes of the "L" nanoantennas can be compensated by the thickness-dependent dispersion of the SiO_2 spacing layer, resulting in a dispersion-free response.[12] Then, we added a VO_2 film above the whole waveplate, so that the optical response of the metasurface can be modified through the phase transition of VO_2. Here, to achieve electrical control of the phase transition of VO_2, we connected the two ends of a silver electrode to external circuitry by using silver conductive paint. A DC power supply was used to apply current to the silver electrode, and the current value in the circuitry was

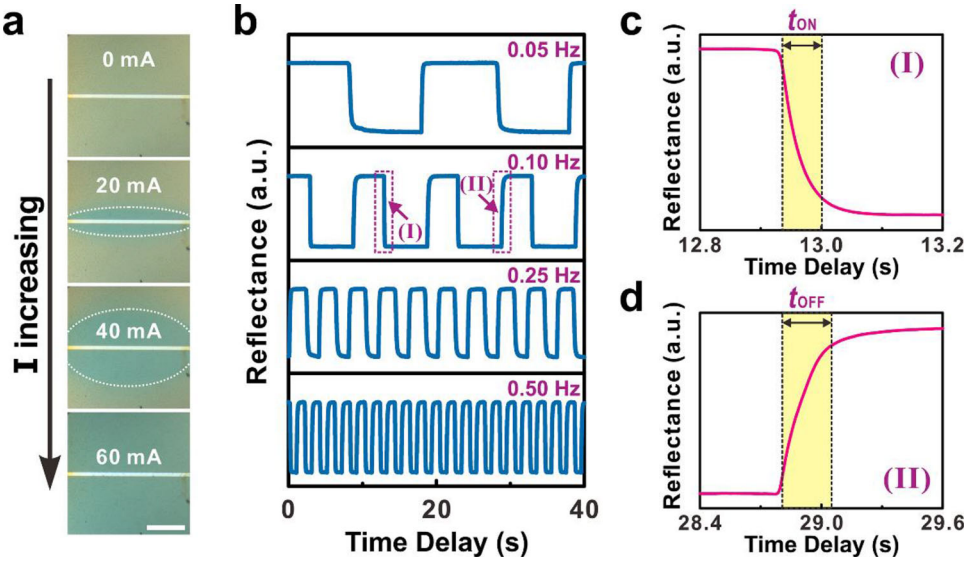

Figure 2. Electrically driven phase transition of a VO_2 film. a) Optical images of 60-nm-thick VO_2 film subjected to different currents. The scale bar is 100 μm. b) Temporal response of electrically tuned phase transition of VO_2 measured at the wavelength of 800 nm. c) A falling edge when the modulation frequency was 0.10 Hz; t_{ON} represents the ON switching time (65 ms). d) A rising edge when the modulation frequency was 0.1 Hz; t_{OFF} represents the OFF switching time (245 ms).

measured by the built-in amperemeter of the DC source. When the electrical current is applied, the phase transition of VO_2 can be induced by the Joule heat. As illustrated in **Figure 2**a, the color of the region around the silver electrode changes with the increase of current, which is attributed to the phase transition of VO_2 induced by the Joule heating, as shown in Figure S1 (Supporting Information). Further, we applied rectangular-shaped current pulses to the sample, and measured the reflectance at the wavelength of 800 nm, as shown in Figure 2b. When a current pulse was applied, the VO_2 was transformed into the metallic phase, leading to the decrease of reflectance. However, when the current pulse was turned off, the VO_2 was transformed back to the insulating phase, and the reflectance returned to its original value. Figure 2c,d shows the falling and rising edges, respectively, when the modulation frequency was 0.1 Hz. Then the ON switching time (t_{ON}) and OFF switching time (t_{OFF}) can be achieved[54] from the time taken for the reflectance decreasing from 90% to 10% of the maximum value or vice versa, respectively. We can find that t_{ON} and t_{OFF} are around 65 and 245 ms, respectively. Compared to the method of direct heating, where both t_{ON} and t_{OFF} are usually more than several seconds, the electrically driven Joule-heat-tuned method demonstrated here can significantly improve the operation speed.

When the input current is lower than a critical value (I_0), VO_2 is an insulator, and a broadband half- or quarter-wave plate can be realized by modifying the geometric parameters of the MIM structure as illustrated in the left panel of Figure 1. If the incident light is *x*-polarized, the reflected wave will be *y*-polarized or circularly polarized depending on the structural parameters. However, when we increase the input current to the critical value I_0, the temperature will rise to above 340 K and VO_2 will transform into a metallic phase. In this case, the infrared light cannot be transmitted through the VO_2 film into the underlying anisotropic plasmonic nanostructure, and the device functions as a broadband mirror as illustrated in the right panel of Figure 1. With the same incident *x*-polarized light, the reflected wave remains *x*-polarized. The electrically tunable broadband waveplate based on the phase transition of VO_2 is reversible. When the current decreases, the VO_2 is transformed back to the insulating phase, and the sample functions as a broadband half- or quarter- wave plate again, as schematically shown in the left panel of Figure 1.

Then, we fabricated the anisotropic metasurface to verify the electrically driven broadband half-wave plate experimentally. The anisotropic metasurface was sequentially fabricated by magnetron sputtering, plasma-enhanced chemical vapor deposition, e-beam lithography, and e-gun evaporation (see the Experimental Section for details). **Figure 3**a is an optical image of the sample, where the distance between the sample and the silver electrode is 100 μm. Figure 3b is the scanning electron microscopy (SEM) image of the same sample. The thickness of the gold (Au) reflection layer and silica (SiO_2) spacing layer were designed to be 100 nm and 550 nm, respectively. The length and width of the Au "L" nanoantenna were set as 900 nm and 200 nm, respectively, and the period of the structure was 1800 nm. The 60 nm VO_2 film completely covered the anisotropic metasurfaces. We calculated the reflection spectrum of the structure using finite-difference time-domain method software (FDTD solutions from Lumerical Inc.) (see the Experimental Section for details). Figure 3c,d presents the simulated reflection spectra of the structure under *x*-polarized incidence with VO_2 in the insulating and metallic phase, respectively. When VO_2 is in the insulating phase, the *x*-polarized reflectance approaches 0 in the wavelength range from 3.5 to 6.75 μm, while the *y*-polarized reflectance is larger than 60% in this wavelength range, as shown in Figure 3c. Therefore, the structure functions as a broadband half-wave plate when VO_2 is in the insulating phase. Because the imaginary part of the permittivity of VO_2 is small in the infrared spectrum when it is in the insulating phase, the infrared light can be transmitted

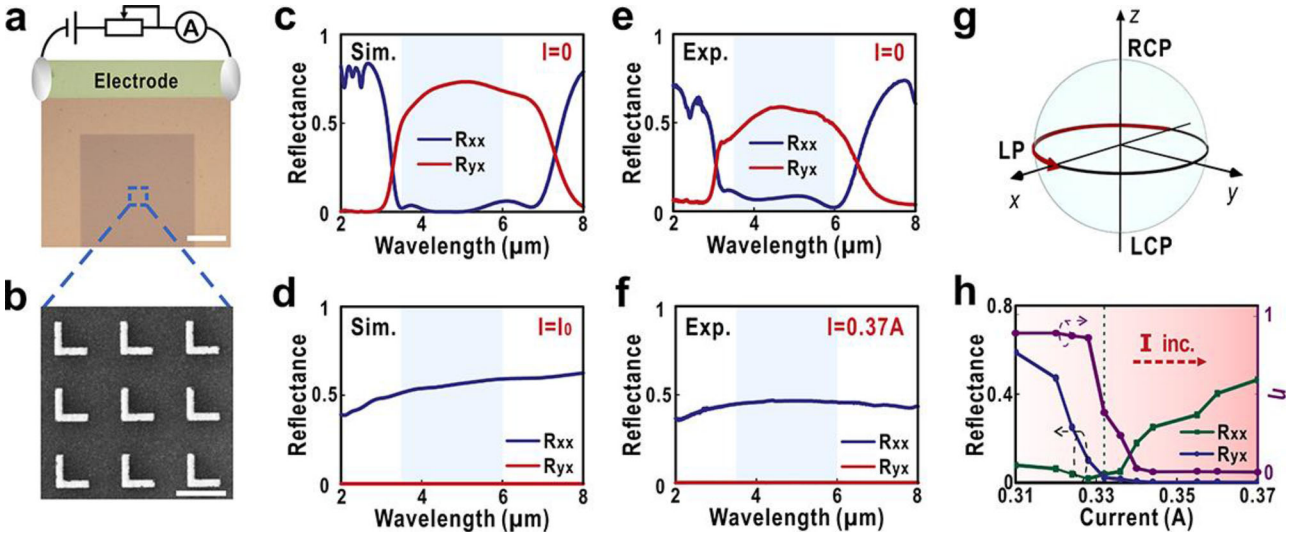

Figure 3. Electrically driven tunable broadband half-wave plate. a) Optical image of the electrically tunable broadband half-wave plate; the scale bar is 100 μm. b) SEM image of the sample in (a); the scale bar is 1500 nm. Simulated reflection spectra of the tunable broadband half-wave plate under *x*-polarized incidence with VO_2 in the c) insulating phase and d) metallic phase, respectively. Measured reflection spectra of the sample under *x*-polarized incidence at e) 0 A and f) 0.37 A, respectively. g) Polarization state of the reflected light plotted schematically in the Poincare sphere. h) Measured reflectivity of the sample under *x*-polarized incidence at a wavelength of 4.7 μm as the current was increased. The sample can work as a half-wave plate when the current is lower than 0.328 A and can be transformed to a mirror when the current is larger than 0.34 A. The transition point is located at 0.332 A or so, as indicated by the dotted line. The polarization conversion efficiency (η) is also evaluated at different applied current.

through the VO_2 film into the underlying anisotropic plasmonic nanostructure and rotate the polarization direction. When VO_2 is in the metallic phase, the *y*-polarized reflectance approaches 0 in the wavelength range from 2 to 8 μm, while the *x*-polarized reflectance is larger than 40% in this wavelength range, as shown in Figure 3d. Therefore, the polarization state of the reflected light is the same as that of the incident light when VO_2 is in the metallic phase. As a result, we can switch the polarization state of the reflected light between a horizontal polarization and a perpendicular polarization through the phase transition of VO_2.

We measured the reflection spectra of the sample at different currents using a Fourier-transform infrared spectrometer (Vertex 70v, Bruker), equipped with focal plane array (FPA). Figure 3e,f presents the measured reflection spectra of the sample under *x*-polarized incidence at 0 and 0.37 A, respectively. When no electrical current is applied, the *x*-polarized reflectance is lower than 10% in the wavelength range from 4 to 6 μm, while the *y*-polarized reflectance is larger than 50% in this wavelength range. The result indicates that the structure indeed acts as a broadband half-wave plate. When the current increases to 0.37 A, the *y*-polarized reflectance approaches 0 in the wavelength range from 2 to 8 μm, while the *x*-polarized reflectance is larger than 40% in this wavelength range. Therefore, the polarization state of the reflected light is the same as that of the incident light. When the current is turned off, the metasurface becomes a broadband half-wave plate again due to the decrease of the temperature, demonstrating the dynamic reversible modulation of the polarization state across a broad wavelength range.

To investigate the intermediate states of the phase transition, we also measured the reflection spectra of the sample under *x*-polarized incidence at several discrete currents ranging from 0 to 0.37 A. Figure 3h shows the measured reflectance of the sample under *x*-polarized incidence at the wavelength of 4.7 μm as the current increases. The results indicate that there are two different processes responsible for the observed variation in reflectance. The reflectance begins to vary at a current of 0.31 A. As the current increases from 0.31 to 0.332 A, the *y*-polarized reflectance significantly decreases while the *x*-polarized reflectance slowly varies. This phenomenon can be attributed to the fact that only a part of the VO_2 above the sample has transformed into the metallic phase. However, when the current is larger than 0.332 A, the *y*-polarized reflection almost disappears, while the *x*-polarized reflectance increases quickly as the current increases. In this case, most of the VO_2 in the sample has transformed into the metallic phase. For currents larger than 0.37 A, both the *x*- and *y*-polarized reflectances remain constant, which means that the VO_2 in the sample has completely transformed into the metallic phase. To illustrate these polarization state variations, we plotted the polarization state of the reflected light in the Poincare sphere as schematically shown in Figure 3g. Under *x*-polarized incidence, the reflected light varies from the *y*-polarized state to the *x*-polarized state as the current continuously increases. The polarization conversion efficiency (η) of this tunable half-wave plate can be evaluated by following the definition[55] $\eta = R_{yx}/(R_{xx} + R_{yx})$, where R_{yx} is the *y*-polarized reflectance under *x*-polarized incidence and R_{xx} is the *x*-polarized reflectance under *x*-polarized incidence, respectively. As shown in Figure 3h, the polarization conversion efficiency reaches ≈85% when the applied current is lower than 0.328 A. When the current is increased around 0.332 A, the VO_2 undergoes the phase transition and the absorbance loss of VO_2 increases obviously during this process.[56] When the current is increased further (larger than 0.34 A), there is no obvious polarization conversion and the device functions as a broadband mirror in this case. As a result, we can produce an

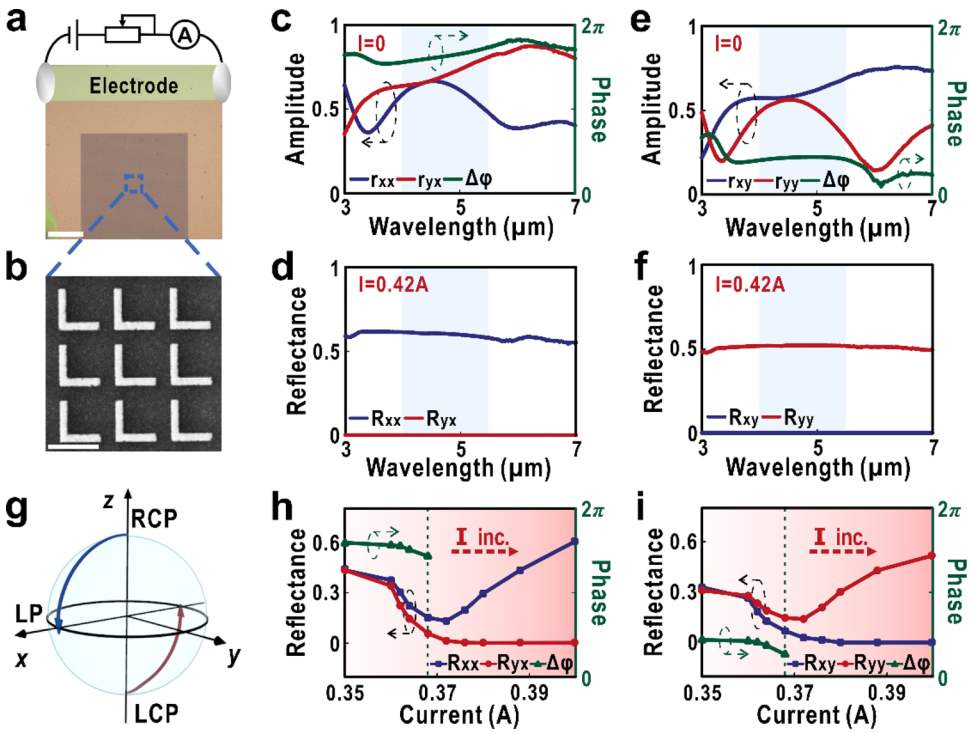

Figure 4. Electrically driven tunable broadband quarter-wave plate. a) Optical image of the electrically tunable broadband quarter-wave plate; the scale bar is 100 μm. b) SEM image of the sample in (a); the scale bar is 1500 nm. Measured reflection spectra of the sample under *x*-polarized incidence at c) 0 A and d) 0.42 A, respectively. Measured reflection spectra of the sample under *y*-polarized incidence at e) 0 A and f) 0.42 A, respectively. g) Polarization state of the reflected light plotted schematically in the Poincare sphere, where the blue and red lines represent the polarization state of incident light along the *x* and *y* direction, respectively. Measured reflectivity and phase of the sample as the current was increased at the wavelength of 4.4 μm under h) *x*-polarized incidence and i) *y*-polarized incidence. The sample can work as a quarter-wave plate when the current is lower than 0.364 A and will be transformed into a mirror when the current is larger than 0.38 A. The transition point is around 0.368 A, as indicated by the dotted line.

electrically tunable broadband half-wave plate by exploiting the phase transition of VO_2, which allows the polarization state to be continuously modulated.

Using the same design principle, we also demonstrated an electrically driven broadband quarter-wave plate. Here, the length of the "L" Au nanoantenna and the period of the array were changed to 1100 and 1530 nm, respectively, while other geometric parameters remained the same as the structure in the half-wave plate. **Figure 4**a shows an optical image of the sample, in which the distance between the sample and the silver-electrode is 100 μm. Figure 4b presents the SEM image of the sample. The measured reflection spectra of the sample under *x*-polarized incidence at 0 and 0.42 A are shown in Figure 4c,d, respectively. The phase difference between the *x*- and *y*-polarized reflection can be measured based on the method presented in our previous work.[12] When no electrical current is applied, the *x*-polarized reflectance is nearly equal to the *y*-polarized reflectance in the wavelength range from 4.15 to 4.65 μm, and the phase difference between the *x*- and *y*-polarized reflection is $\approx 1.5\pi$ in this wavelength range. Hence, the reflected light is changed to right-hand circularly polarized (RCP) light under *x*-polarized incidence. At the applied current of 0.42 A, the *y*-polarized reflectance approaches 0 in the wavelength range from 3 to 7 μm, while the *x*-polarized reflectance is larger than 50% in this wavelength range. Hence, the polarization state of the reflected light is the same as that of the incident light at the applied current of 0.42 A. We also measured the reflection spectra of the sample under *y*-polarized incidence at 0 and 0.42 A, as shown in Figure 4e,f, respectively. Similar to the case *x*-polarized incidence, under *y*-polarized incidence, the reflected light becomes left-hand circularly polarized (LCP) at 0 A and remains the same as the incident light at 0.42 A. When we turn off the current, the structure becomes a broadband quarter-wave plate again due to the dissipation of Joule heat. These experimental results reasonably agree with the simulated ones (Figure S2, Supporting Information).

Figure 4h shows the measured reflectance and phase difference of the sample under *x*-polarized incidence at a wavelength of 4.4 μm when the electrical current is continuously changed. The reflectance and phase difference begin to change when the electrical current reaches 0.35 A. As the current increases from 0.35 to 0.364 A, the *x*- and *y*-polarized reflectance decrease simultaneously, while the phase difference between the *x*- and *y*-polarized reflectance remain approximately 1.5π. This result indicates that the sample works as a quarter-wave plate, which transforms an *x*-polarized incident light to a RCP light. The operation efficiency of a quarter-wave plate can be evaluated by the power ratio between the reflected and incident light.[16] It is found that the operation efficiency of this quarter-wave plate can reach a maximum of 86% at a current of 0.35 A. As the current increases from 0.364 to 0.38 A, the absorbance loss of the device increases obviously because VO_2 undergoes to the insulator-to-metal phase transition.[56] When the current develops more than 0.38 A, the

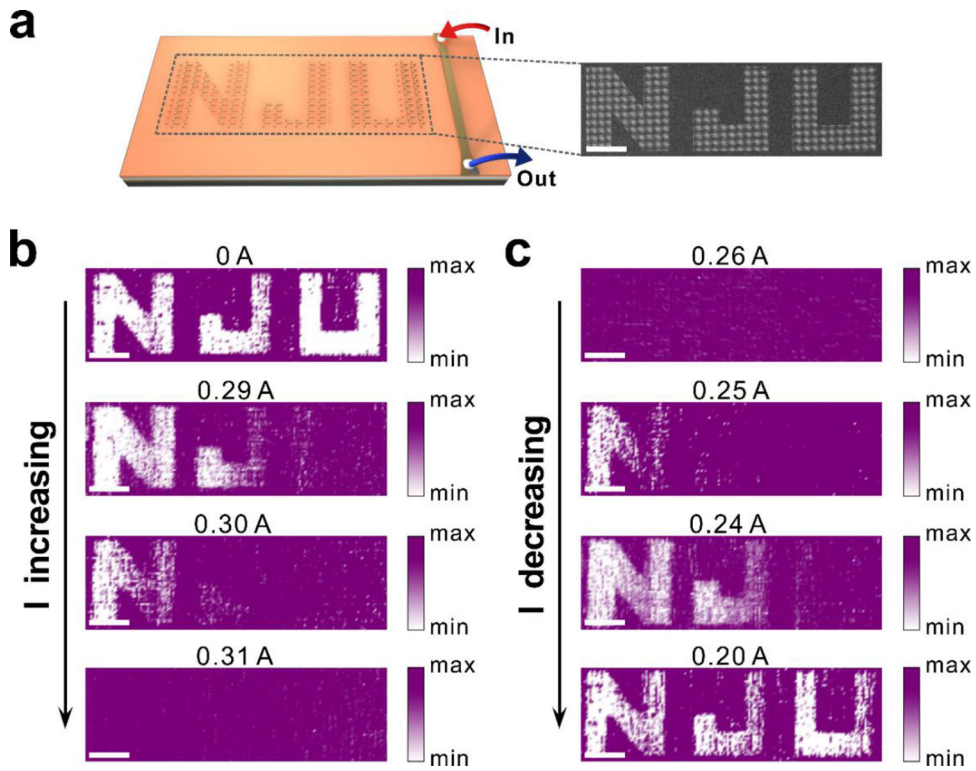

Figure 5. Electrically controlled reversible polarization scanning display. a) Schematic of the electrically tunable infrared image of an "NJU" pattern, where the region within the "NJU" is composed of periodic "L" nanoantenna arrays with the same structural parameters as the sample in Figure 3, whereas the region outside the "NJU" does not contain any periodic "L" nanoantenna arrays. The red arrow represents the input of currents, whereas the blue arrow represents the output of currents. Inset: the SEM image of a sample; the scale bar is 100 μm. b) FPA image of the sample at increasing currents of 0, 0.29, 0.30, and 0.31 A. c) FPA image of the sample at decreasing currents of 0.26, 0.25, 0.24, and 0.20 A; all scale bars are 100 μm.

y-polarized reflectance almost disappears, while the *x*-polarized reflectance rises gradually as the current boosts. In this case, the device functions as a broadband mirror and the operation efficiency can reach ≈60% at a current of 0.4 A. To illustrate how the polarization state varies directly with the current, we plot the polarization states of the reflected light in a Poincare sphere (blue curve), as schematically shown in Figure 4g. Under *x*-polarized incidence, the reflected light changes from a right-hand circular polarization state to an *x*-polarized state as the current is continuously increased.

Figure 4i shows the measured reflectance and phase difference of the sample under *y*-polarized incidence at a wavelength of 4.4 μm over a certain range of applied electrical currents. The reflectance and phase difference begin to change when the applied current reaches 0.35 A, similar to what was demonstrated for the *x*-polarized incidence. As the electrical current increases from 0.35 to 0.364 A, the device also functions as a quarter-wave plate, transforming a *y*-polarized incident light to a LCP light. In this case, the operation efficiency of the quarter-wave plate reaches ≈64% when the applied current is 0.35 A. As the current increases from 0.364 to 0.38 A, the VO_2 undergoes the phase transition, and the absorption loss increases obviously.[56] When the current exceeds 0.38 A, the *x*-polarized reflectance almost disappears, while the *y*-polarized reflectance rises gradually as the current increases. In this case, the device functions as a broadband mirror and the operation efficiency reaches a maximum of 52% at the applied current of 0.4 A. We also plot the polarization states of the reflected light in a Poincare sphere, as the red curve shown in Figure 4g. Under a *y*-polarized incidence, the reflected light changes from a left-hand circular polarization state to a *y*-polarized state. Accordingly, we have realized an electrically driven tunable broadband quarter-wave plate by using the phase transition of VO_2.

2.2. Electrically Controlled Reversible Polarization Scanning Display

We have implemented electrically tunable broadband waveplates by integrating VO_2 with anisotropic metasurfaces. To further demonstrate the reversible and continuous modulation of the polarization state, a unique scanning infrared display was designed. An "NJU" pattern was created, as shown in **Figure 5**a. The region within the "NJU" pattern is composed of periodic "L" nanoantenna arrays with the same structural parameters as the sample in Figure 3, whereas the region outside the "NJU" does not contain any periodic "L" nanoantenna arrays. We added a 50-nm-thick silver electrode on the right side of the "NJU," and the distance between the "NJU" and the silver electrode was around 100 μm. We measured the FPA images of the sample at a wavelength of 4.7 μm, and the optical axes of both the polarizer and analyzer were oriented along the *x*-direction. As we have discussed,

when the electrical current is zero, VO_2 is in an insulating phase and the periodic "L" pattern acts as a half-wave plate. The incident *x*-polarized light can be converted into a *y*-polarized component with high efficiency. However, the light remains *x*-polarized outside the "NJU" region. With the analyzer, the reflectance is nearly zero within the "NJU" region while it is high outside. Therefore, in the FPA image taken at 0 A, we can clearly observe the "NJU" pattern, as shown in Figure 5b. When we increase the input current, the generated Joule heat produces a specific temperature distribution, which decreases from the right side (the position of the silver electrode) to the left side.

Next, we carefully adjusted the input electric current to 0.29 A. In this case, the VO_2 in the "U" region was transformed into a metallic state while the VO_2 in the "NJ" region remained unchanged. Therefore, the metasurface in the "U" region was turned into a broadband mirror and the polarization state of the reflected light was similar to that observed in the region outside the "NJU" pattern. The reflectance within and outside the "U" region was almost identical. Consequently, at a current of 0.29 A, we can only see the "NJ" pattern in the FPA image, as shown in Figure 5b. When the current was further increased to 0.3 A, the VO_2 in the "J" region was also transformed into a metallic state. Therefore, the "J" in the pattern disappeared and we can only see the "N" in the FPA image. Finally, when the current was increased to 0.31 A, all the VO_2 in the "NJU" region become a metallic state, and the reflection in the whole sample exhibited the same polarization state. Therefore, we cannot see any pattern in the FPA image. Moreover, the polarization scanning display can be reversed by varying the current. As shown in Figure 5c, when the input current was slowly decreased from 0.31 to 0.20 A, the "NJU" pattern re-emerged from the left to the right side, just like the reverse of the process shown in Figure 5b. This demonstrates that we can produce a dynamically reversible polarization scanning display device based on the electrically controlled continuous phase transition of VO_2.

It is worthwhile to mention that, compared with previous studies in which the patterns were only able to be displayed and erased integrally,[22,51,52] our demonstration proposes a novel scanning display and erasure method based on the precise electric tunability of the phase transition. The electrically controlled reversible polarization scanning display allows the pattern information to be easily displayed and erased reversibly, which could be applied to dynamic display devices, anti-counterfeit labels, and so on. The display image is also a significant information carrier which can directly describe the objective world in addition to the information world. For instance, some dynamic metasurface holograms have already been utilized for advanced optical information processing and encryption.[57] Similarly, FPA images from polarization scanning display devices also have the ability to store information. Sets of geometric codes could be displayed using our devices instead of the "NJU" pattern, which could potentially be used for optical information processing and encryption.

2.3. Independent Control of Multiple Polarization Display

On the basis of active modulation of infrared light, we further propose a platform to implement the independent modulation of multiple polarization display. We consider *N* independent patterns, in which the polarization state of reflected light can be controlled by *N* independent switches. The polarization state of reflected light for each pattern can be defined as "0" or "1" corresponding to "on" or "off" state of each switch. Therefore, the whole sample can support 2^N display states and every state can display different infrared images.

In order to confirm this idea, we designed three different patterns including "apple," "butterfly," and "chick," as shown in **Figure 6**a. The region within these patterns is composed of periodic "L" nanoantenna arrays with the same structural parameters as the sample in Figure 3, whereas the region without these patterns does not contain any periodic "L" nanoantenna arrays. We added a 50-nm-thick silver electrode in the vicinity of each pattern, where the distance between each pattern and the corresponding silver electrode is around 100 μm. To avoid the effect of heat cross-talk, we cut the sample into three independent parts, each containing an "apple," "butterfly," or "chick" pattern. We measured the FPA images of these samples at the wavelength of 4.7 μm, with the optical axis of both the polarizer and analyzer set along the *x*-direction. The measured FPA images are shown in Figure 6b. In the absence of electric current, which can be defined as the "1" state, the VO_2 is in an insulator state and these patterns act as a half-wave plate. The reflected light in these patterns is *y*-polarized, whereas the reflected light outside these patterns is still *x*-polarized. As the analyzer is set along the *x*-direction, the reflectance is low inside the patterns, while high outside the patterns. Therefore, we can clearly see these patterns from the FPA image. However, when current is applied, which can be defined as the "0" state, VO_2 is transformed into a metallic state. The reflected light both inside and outside these patterns is *x*-polarized with almost identical amplitude. Therefore, we cannot see these patterns on the FPA images. By selectively applying current, we can achieve eight different states, which can be encoded as "111," "110," "101," "100," "011," "010," "001," and "000." Each state displays a different infrared image, as shown in Figure 6b.

As we know, dynamic multiplexing can be used for metahologram, where different holographic images can be realized by controlling the structured laser beam to open different space channels.[58] As shown in Figure 6, the independent modulation of multiple polarization display can be regarded as a dynamic multiplexing polarization display, where different patterns correspond to different space channels and the different polarization display can be realized by controlling the current. The entire sample is divided into *N* different patterns, and the polarization display of each pattern can be switched by turning on or off the corresponding electrical currents. The entire sample is able to show different images by selectively applying electrical currents, which demonstrates a dynamic display with 2^N encoding states ($N = 3$ in our current experiments). As a result, we realize the dynamic multiplexing polarization display and show the polarization encoding display using the electrically tunable broadband waveplates.

The study is a proof-of-concept demonstration of coding-metasurfaces, which have been introduced to build up a connection between the physical world and the information world.[27,59,60] Based on the independent control of the polarization states, reconfigurable coding-metasurfaces that operate over a range from 3.5 to 6 μm is possible. Through the current-controlled phase transition of vanadium dioxide, the unit cell can

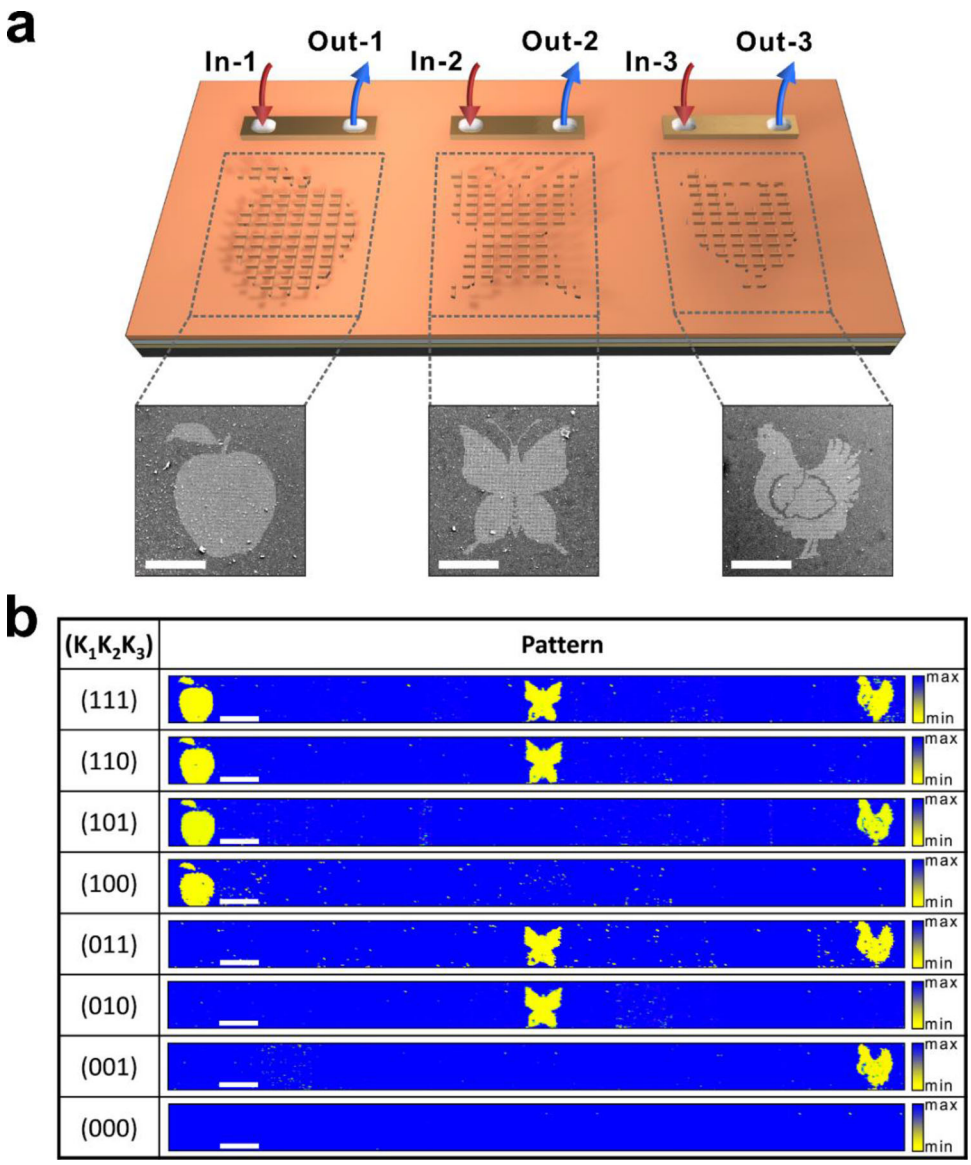

Figure 6. Demonstration of the independent control of the polarization display. a) Upper section shows three different patterns of "apple," "butterfly," and "chick," respectively. These patterns are composed of periodic "L" nanoantenna arrays with the same structural parameters as the sample in Figure 3. The red arrows represent the input of currents, whereas the blue arrows represent the output of currents. The lower section shows three selected SEM images of a sample; all scale bars are 100 μm. b) FPA images of the sample; all scale bars are 200 μm. When there was no current, this was defined as the "1" state, while if the current was applied, it was defined as the "0" state. By selectively applying the current, eight different states can be realized, which can be encoded as "111," "110," "101," "100," "011," "010," "001," and "000."

be switched between elements "0" and "1," corresponding to two orthogonal polarization states of reflected light. We believe that there are many applications of this technology, such as in signal processing, information communications, and data storage. Furthermore, our experimental results provide a new paradigm to accurately control the polarization state distribution of spatial light as a result of precise on-chip modification of the optical response of phase transition materials. We expect that the results of this study can be used in the future development of applications such as 3D video projection, augmented reality, and adaptive optics.

3. Conclusion

In conclusion, we demonstrate the electrically driven polarization states that are able to operate across a broad wavelength range by integrating VO_2 with dispersion-free metasurfaces. Based on the Joule-heat-induced phase transition of VO_2, the polarization state of the reflected light can be continuously tuned from a horizontal polarization to a perpendicular polarization or from circular polarization to linear polarization, depending on the structural parameters. Moreover, based on the dynamically tunable polarization states, an electrically reversible polarization

scanning display with a precisely controlled input current has been demonstrated. Finally, we demonstrate the ability to dynamically and independently control multiple polarization display, and we successfully produce eight different infrared images by selectively modifying the current, which demonstrates a dynamic display with 2^N encoding states ($N = 3$ in current experiments), realizing the dynamic multiplexing polarization display. Although in this work we focus on the electrically tunable broadband polarization states in the infrared spectrum, we can adjust the geometric parameters of metasurfaces to operate in other wavelength ranges. In particular, as the phase transition of VO_2 can be triggered via light over subpicosecond timescales,[50] the polarization state of the reflected light could be tuned rapidly. Therefore, we anticipate that the electrically driven broadband polarization states can be applied to information transmission, microscopy, and polarimetric imaging.

4. Experimental Section

Fabrication of Samples: The metasurfaces were fabricated on silicon substrates. Frist, 100-nm-thick gold (Au) and 550-nm-thick silicon oxide (SiO_2) films were deposited on the substrate by magnetron sputtering and plasma-enhanced chemical vapor deposition (PECVD), respectively. The 50-nm-thick periodic "L" nanoantenna arrays were fabricated on top of the Au/SiO_2 layer using e-beam lithography and a lift-off process. An annealing process in an oxygen atmosphere was then performed after e-gun evaporation of the V film to produce the 60-nm-thick VO_2 layer. Then, 50-nm-thick silver electrodes were fabricated on the VO_2 film using maskless ultraviolet lithography and a lift-off process.

Optical and Electrical Measurements: The reflection spectra and the FPA images of the samples were measured using the single element and FPA modules of a Fourier-transform infrared (FTIR) system (Vertex 70v, Bruker), respectively. Each unit in the FPA image represents a 200 μm × 200 μm region of the sample which was photographed using a 256 × 256 focal plane array detector of the FTIR system. To achieve electrical control of the samples, electrodes were prepared on the two ends of the silver electrodes by using silver conductive paint to connect to external circuitry. A DC power supply was used to apply current to the silver electrodes. The current value in the circuitry was measured using the built-in amperemeter of the DC source.

Numerical Simulations: The simulated reflection spectra were performed using finite-difference time-domain method software (FDTD Solutions, Lumerical Inc.). Periodic boundary conditions were applied to the unit structures in the simulations. The refractive indices of the VO_2 thin film in the insulating phase and metallic phase were extracted from the literature.[61] The refractive indices of SiO_2 and Au were extracted from the literature.[62] Numerical calculations of the temperature distributions were carried out using COMSOL MULTIPHYSICS, a commercial software package based on the finite element method.

Supporting Information

Supporting Information is available from the Wiley Online Library or from the author.

Acknowledgements

This work was supported by the National Key R&D Program of China (2020YFA0211300 and 2017YFA0303702) and the National Natural Science Foundation of China (11634005, 61975078, 11674155, and 11974177). Y.L. acknowledges the financial support from the National Science Foundation (ECCS-1916839).

Conflict of Interest

The authors declare no conflict of interest.

Author Contributions

F.-Z.S. and J.-N.W. contributed equally to this work. R.W.P., F.Z.S., and M.W. conceived this work. F.Z.S., J.N.W., and Y.J.G. fabricated the samples. F.Z.S. and J.N.W. performed the optical measurements. F.Z.S., B.X., R.H.F., and D.X.Q. carried out the simulations. F.Z.S., J.N.W., B.X., R.W.P., Y.L., and M.W. wrote the paper. R.W.P., Y.L., and M.W. directed the experiment. R.W.P., Y.L., and M.W. organized the project, designed experiments, analyzed the results, and prepared the paper. All authors discussed the results and commented on the paper.

Data Availability Statement

Research data are not shared.

Keywords

active metasurfaces, electrically tuning broadband polarization states, electrically tuned phase-change materials

Received: March 19, 2021
Revised: June 7, 2021
Published online:

[1] A. V. Kildishev, A. Boltasseva, V. M. Shalaev, *Science* **2013**, *339*, 1232009.
[2] N. Yu, F. Capasso, *Nat. Mater.* **2014**, *13*, 139.
[3] G. Zheng, H. Mühlenbernd, M. Kenney, G. Li, T. Zentgraf, S. Zhang, *Nat. Nanotechnol.* **2015**, *10*, 308.
[4] M. Khorasaninejad, F. Capasso, *Science* **2017**, *358*, eaam8100.
[5] Z.-H. Wang, Y.-S. Hu, X. Xiong, R.-W. Peng, M. Wang, *Opt. Lett.* **2017**, *42*, 1153.
[6] F. Ding, A. Pors, S. I. Bozhevolnyi, *Rep. Prog. Phys.* **2018**, *81*, 026401.
[7] R. Zhao, L. Huang, C. Tang, J. Li, X. Li, Y. Wang, T. Zentgraf, *Adv. Opt. Mater.* **2018**, *6*, 1800490.
[8] N. Yu, F. Aieta, P. Genevet, M. A. Kats, Z. Gaburro, F. Capasso, *Nano Lett.* **2012**, *12*, 6328.
[9] A. Pors, M. G. Nielsen, S. I. Bozhevolnyi, *Opt. Lett.* **2013**, *38*, 513.
[10] N. K. Grady, J. E. Heyes, D. R. Chowdhury, Y. Zeng, M. T. Reiten, A. K. Azad, A. J. Taylor, D. A. R. Dalvit, H.-T. Chen, *Science* **2013**, *340*, 1304.
[11] Q. Lévesque, M. Makhsiyan, P. Bouchon, F. Pardo, J. Jaeck, N. Bardou, C. Dupuis, R. Haïdar, J.-L. Pelouard, *Appl. Phys. Lett.* **2014**, *104*, 111105.
[12] S.-C. Jiang, X. Xiong, Y.-S. Hu, Y.-H. Hu, G.-B. Ma, R.-W. Peng, C. Sun, M. Wang, *Phys. Rev. X* **2014**, *4*, 021026.
[13] L. Kang, R. P. Jenkins, D. H. Werner, *Adv. Opt. Mater.* **2019**, *7*, 1801813.
[14] T. Cui, B. Bai, H.-B. Sun, *Adv. Funct. Mater.* **2019**, *29*, 1806692.
[15] A. M. Shaltout, V. M. Shalaev, M. L. Brongersma, *Science* **2019**, *364*, eaat3100.
[16] Z. Miao, Q. Wu, X. Li, Q. He, K. Ding, Z. An, Y. Zhang, L. Zhou, *Phys. Rev. X* **2015**, *5*, 041027.
[17] Z. Su, F. Cheng, L. Li, Y. Liu, *ACS Photonics* **2019**, *6*, 1947.
[18] W. Ma, Z. Huang, X. Bai, P. Zhan, Y. Liu, *ACS Photonics* **2017**, *4*, 1770.

[19] Y. Yang, K. Kelley, E. Sachet, S. Campione, T. S. Luk, J.-P. Maria, M. B. Sinclair, I. Brener, *Nat. Photonics* **2017**, *11*, 390.
[20] L. H. Nicholls, F. J. Rodríguez-Fortuño, M. E. Nasir, R. M. Córdova-Castro, N. Olivier, G. A. Wurtz, A. V. Zayats, *Nat. Photonics* **2017**, *11*, 628.
[21] M.-X. Ren, W. Wu, W. Cai, B. Pi, X.-Z. Zhang, J.-J. Xu, *Light: Sci. Appl.* **2017**, *6*, e16254.
[22] Z.-Y. Jia, F.-Z. Shu, Y.-J. Gao, F. Cheng, R.-W. Peng, R.-H. Fan, Y. Liu, M. Wang, *Phys. Rev. Appl.* **2018**, *9*, 034009.
[23] X. Duan, N. Liu, *ACS Nano* **2018**, *12*, 8817.
[24] B. Kang, J. H. Woo, E. Choi, H.-H. Lee, E. S. Kim, J. Kim, T.-J. Hwang, Y.-S. Park, D. H. Kim, J. W. Wu, *Opt. Express* **2010**, *18*, 16492.
[25] A. Komar, R. Paniagua-Domínguez, A. Miroshnichenko, Y. F. Yu, Y. S. Kivshar, A. I. Kuznetsov, D. Neshev, *ACS Photonics* **2018**, *5*, 1742.
[26] S.-Q. Li, X. Xu, R. M. Veetil, V. Valuckas, R. Paniagua-Domínguez, A. I. Kuznetsov, *Science* **2019**, *364*, 1087.
[27] L. Li, T. J. Cui, *Nanophotonics* **2019**, *8*, 703.
[28] R.-H. Fan, Y. Zhou, X.-P. Ren, R.-W. Peng, S.-C. Jiang, D.-H. Xu, X. Xiong, X.-R. Huang, M. Wang, *Adv. Mater.* **2015**, *27*, 1201.
[29] M. T. Nouman, J. H. Hwang, M. Faiyaz, K.-J. Lee, D.-Y. Noh, J.-H. Jang, *Opt. Express* **2018**, *26*, 12922.
[30] F.-Z. Shu, F.-F. Yu, R.-W. Peng, Y.-Y. Zhu, B. Xiong, R.-H. Fan, Z.-H. Wang, Y. Liu, M. Wang, *Adv. Opt. Mater.* **2018**, *6*, 1700939.
[31] Y.-W. Huang, H. W. H. Lee, R. Sokhoyan, R. A. Pala, K. Thyagarajan, S. Han, D. P. Tsai, H. A. Atwater, *Nano Lett.* **2016**, *16*, 5319.
[32] S. C. Malek, H. S. Ee, R. Agarwal, *Nano Lett.* **2017**, *17*, 3641.
[33] P. Yu, J. Li, S. Zhang, Z. Jin, G. Schütz, C.-W. Qiu, M. Hirscher, N. Liu, *Nano Lett.* **2018**, *18*, 4584.
[34] Z. Yang, C. Ko, S. Ramanathan, *Annu. Rev. Mater. Res.* **2011**, *41*, 337.
[35] K. Liu, S. Lee, S. Yang, O. Delaire, J. Wu, *Mater. Today* **2018**, *21*, 875.
[36] F. J. Morin, *Phys. Rev. Lett.* **1959**, *3*, 34.
[37] M. Nakano, K. Shibuya, D. Okuyama, T. Hatano, S. Ono, M. Kawasaki, Y. Iwasa, Y. Tokura, *Nature* **2012**, *487*, 459.
[38] J. Jeong, N. Aetukuri, T. Graf, T. D. Schladt, M. G. Samant, S. S. P. Parkin, *Science* **2013**, *339*, 1402.
[39] H. Ma, J. Hou, X. Wang, J. Zhang, Z. Yuan, L. Xiao, Y. Wei, S. Fan, K. Jiang, K. Liu, *Nano Lett.* **2017**, *17*, 421.
[40] T. Wang, D. Torres, F. E. Fernández, C. Wang, N. Sepúlveda, *Sci. Adv.* **2017**, *3*, e1602697.
[41] S.-Y. Li, G. A. Niklasson, C. G. Granqvist, *Thin Solid Films* **2012**, *520*, 3823.
[42] T. Driscoll, H.-T. Kim, B.-G. Chae, B.-J. Kim, Y.-W. Lee, N. M. Jokerst, S. Palit, D. R. Smith, M. D. Ventra, D. N. Basov, *Science* **2009**, *325*, 1518.
[43] M. Liu, H. Y. Hwang, H. Tao, A. C. Strikwerda, K. Fan, G. R. Keiser, A. J. Sternbach, K. G. West, S. Kittiwatanakul, J. Lu, S. A. Wolf, F. G. Omenetto, X. Zhang, K. A. Nelson, R. D. Averitt, *Nature* **2012**, *487*, 345.
[44] D. W. Ferrara, J. Nag, E. R. MacQuarrie, A. B. Kaye, R. F. Haglund, *Nano Lett.* **2013**, *13*, 4169.
[45] J. Rensberg, S. Zhang, Y. Zhou, A. S. McLeod, C. Schwarz, M. Goldflam, M. Liu, J. Kerbusch, R. Nawrodt, S. Ramanathan, D. N. Basov, F. Capasso, C. Ronning, M. A. Kats, *Nano Lett.* **2016**, *16*, 1050.
[46] A. Joushaghani, J. Jeong, S. Paradis, D. Alain, J. S. Aitchison, J. K. S. Poon, *Opt. Express* **2015**, *23*, 3657.
[47] S. Kumar, M. D. Pickett, J. P. Strachan, G. Gibson, Y. Nishi, R. S. Williams, *Adv. Mater.* **2013**, *25*, 6128.
[48] J. del Valle, P. Salev, F. Tesler, N. M. Vargas, Y. Kalcheim, P. Wang, J. Trastoy, M.-H. Lee, G. Kassabian, J. G. Ramírez, M. J. Rozenberg, I. K. Schuller, *Nature* **2019**, *569*, 388.
[49] J. Cao, E. Ertekin, V. Srinivasan, W. Fan, S. Huang, H. Zheng, J. W. L. Yim, D. R. Khanal, D. F. Ogletree, J. C. Grossman, J. Wu, *Nat. Nanotechnol.* **2009**, *4*, 732.
[50] A. Cavalleri, C. Tóth, C. W. Siders, J. A. Squier, F. Ráksi, P. Forget, J. C. Kieffer, *Phys. Rev. Lett.* **2001**, *87*, 237401.
[51] L. Liu, L. Kang, T. S. Mayer, D. H. Werner, *Nat. Commun.* **2016**, *7*, 13236.
[52] Z. Zhu, P. G. Evans, R. F. Haglund, J. G. Valentine, *Nano Lett.* **2017**, *17*, 4881.
[53] Y. Kim, P. C. Wu, R. Sokhoyan, K. Mauser, R. Glaudell, G. K. Shirmanesh, H. A. Atwater, *Nano Lett.* **2019**, *19*, 3961.
[54] W. Tian, T. Zhai, C. Zhang, S. L. Li, X. Wang, F. Liu, D. Liu, X. Cai, K. Tsukagoshi, D. Golberg, Y. Bando, *Adv. Mater.* **2013**, *25*, 4625.
[55] F. Ding, Z. Wang, S. He, V. M. Shalaev, A. V. Kildishev, *ACS Nano* **2015**, *9*, 4111.
[56] M. A. Kats, D. Sharma, J. Lin, P. Genevet, R. Blanchard, Z. Yang, M. M. Qazilbash, D. N. Basov, S. Ramanathan, F. Capasso, *Appl. Phys. Lett.* **2012**, *101*, 221101.
[57] J. Li, S. Kamin, G. Zheng, F. Neubrech, S. Zhang, N. Liu, *Sci. Adv.* **2018**, *4*, eaar6768.
[58] H. Gao, Y. Wang, X. Fan, B. Jiao, T. Li, C. Shang, C. Zeng, L. Deng, W. Xiong, J. Xia, M. Hong, *Sci. Adv.* **2020**, *6*, eaba8595.
[59] C. D. Giovampaola, N. Engheta, *Nat. Mater.* **2014**, *13*, 1115.
[60] T. J. Cui, M. Q. Qi, X. Wan, J. Zhao, Q. Cheng, *Light: Sci. Appl.* **2014**, *3*, e218.
[61] H. W. Verleur, A. S. Barker, C. N. Berglund, *Phys. Rev.* **1968**, *172*, 788.
[62] E. D. Palik, *Handbook of Optical Constants of Solids*, Academic, San Diego, CA **1985**.